scientific reports

Check for updates

OPEN

Retained introns in phototransduction genes of 5xFAD mouse retina suggest vision impairment as an early diagnostic marker for Alzheimer's disease

Hyun-Min Lee[1,4], Jinho Kim[1,4], Ji-Young Kim[1,4], Mi-Jin An[1], Geun-Seup Shin[1], Ah-Ra Jo[1], Yuna Park[1], Chul-Hong Kim[1], Yujeong Hwangbo[1], Ju-Hyun Lee[1], Tae Kyung Hong[1], Kun Ho Lee[2,3], Sangmyung Rhee[1] & Jung-Woong Kim[1]✉

Alzheimer's disease (AD) is an age-related neurodegenerative disorder characterized by neuronal and synaptic loss in the brain, which leads to cognitive impairment and dementia. Therefore, early diagnosis by employing various biomarkers is crucial for preventing and treating AD. Although retinal pathology is an emerging biomarker associated with AD, detailed molecular mechanisms of retinal impairments remain unclear. Herein, we identified genome-wide dysfunction of alternative splicing in the early stage of 5xFAD transgenic mouse retina by performing RNA sequencing analysis. Notably, retained introns, highly enriched in phototransduction and retinal genes in the 1.5-month-old 5xFAD mouse retina, was significantly associated with physiological impairment of rod photoreceptors in the retina, as evidenced by electroretinogram (ERG) analysis. These results indicate that the abnormal scotopic ERG associated with global splicing impairment may be valuable as an early-detection biomarker for AD.

Keywords Alzheimer's disease (AD), Retina, Alternative splicing, Retained intron, 5xFAD

Alzheimer's disease (AD) is a complex neurodegenerative disorder that leads to a gradual decline in cognitive functions, such as memory and behavior[1,2]. Although aging is the most notable risk factor for AD, the rate and extent of cognitive decline varies between individuals, influenced by environmental factors, personal experiences, and genetic predispositions[3]. Epigenetic changes and abnormal RNA splicing events at various AD susceptibility loci may contribute to the onset of AD in healthy brains[4,5]. With advances in transcriptomic and epigenomic technologies, potential neurodegenerative alterations in the AD brain can be detected based on evidence such as downregulation of neuronal functions and upregulation of the innate immune response[6–8]. Employing these approaches could aid in comprehensively clarifying alterations in gene expression regulation in the AD brain, revealing pathophysiology and potential therapeutic options[9]. Identifying molecular alterations as a biomarker in the brain of a living individual prior to AD development remains challenging. Nonetheless, ongoing efforts to develop non-invasive methods for early AD diagnosis without causing damage to the brain tissue are hindered by considerable hurdles.

Alternative splicing (AS) is a regulatory mechanism that can markedly enhance proteome diversity by generating multiple mRNA transcripts from a single gene[10]. Disruptions in splicing patterns are frequently observed during normal aging and may be linked to susceptibility to various diseases, including cancers, cardiovascular disease, and several neuropathies[11,12]. Retained intron (RI) is a type of AS that is garnering interest in human health and disease investigations. RI occurs when an intron is inappropriately retained from the pre-mRNA transcript, leading to intron sequences remaining in the mature mRNA. RI in the brain affects gene expression and protein production and has been implicated in the development of age-related diseases such as Parkinson's disease and AD[13,14]. Amyloid beta (Aβ) deposition is not limited to the brain and can occur

[1]Department of Life Science, Chung-Ang University, 84 Heukseok-Ro, Dongjak-Gu, Seoul 06974, Republic of Korea. [2]Gwangju Alzheimer's & Related Dementia Cohort Research Center, Chosun University, Gwangju 61452, Republic of Korea. [3]Department of Biomedical Science, Chosun University, Gwangju 61452, Republic of Korea. [4]Hyun-Min Lee, Jinho Kim and Ji-Young Kim contributed equally to this work. ✉email: jungkim@cau.ac.kr

in various tissues and organs, including the bone, heart, and retina, contributing to a range of diseases and conditions beyond AD[15–17]. However, the correlation between splicing patterns and physiological functions in Aβ-deposited tissues remains poorly understood.

The retina is a part of the central nervous system, and its structure and functions share several similarities with those of the brain[18]. Owing to the homology between the retina and the brain, AD researchers have focused on the retina as a "window into the brain"[18,19]. Some classic ocular diseases exhibit neurodegenerative mechanisms similar to those in central nervous system disorders[20]. For instance, structural degeneration in the retinal nerve fiber layer at an early stage of AD[21,22], visual dysfunction in AD[23,24], Aβ deposition in five-familial AD (5xFAD) mouse retina[25,26], and apoptosis pathway and photoreceptor degeneration induced by Aβ[27–30] have been reported. The retina can be considered a basic model of the brain, as certain pathological alterations and therapeutic approaches observed in the retina may have relevance or applicability to the brain.

In this study, we performed RNA sequencing (RNA-seq) analysis to compare the retinal transcriptomes of 1.5- and 6-month-old C57BL/6 J and 5xFAD transgenic mice. We observed that the photoreceptor cell-maintenance and AD-related genes were upregulated in 1.5-month-old 5xFAD mouse retinas. Interestingly, we detected a global increase in the RI events in 1.5-month-old 5xFAD mouse retinas. The genes with elevated RI were correlated with visual perception and the maintenance process of photoreceptors. Furthermore, physiological retinal functions of phototransduction were impaired in 1.5-month-old 5xFAD mouse retinas. Our results suggest that a global increase of RI may be a transcriptional signature of early-onset, AD-like amyloidosis and support other clinical studies regarding visual dysfunction in patients with early-stage AD.

Methods

Animals

5xFAD mice, which carry human *APP* (K670N/M671L + I716V + V717I) and *PSEN1* (M146L + L286V) transgenes, were obtained from Jackson Laboratory (Tg6799; MMRRC Stock #034848). To maintain a consistent C57BL/6 J genetic background, the 5xFAD line was maintained by backcrossing male C57BL/6 J wild-type (WT) mice with female 5xFAD transgenic mice for more than seven generations, following the supplier's recommendations. For all experiments, we used male hemizygous 5xFAD mice and age-matched male WT littermates, weighing 20–27 g and aged either 1.5 or 6 months. The number of animals used per group was n = 3–5 depending on the experiment, and specific n values are provided in each figure legend. The animals were housed under a controlled 12-h light/dark cycle, with lights off at 20:00. They were provided ad libitum access to food (5053 PicoLab® Rodent Diet 20, Labdiet, USA) and water. Weaning occurred at 3 weeks of age, and mice were housed in same-sex groups of 1–6 per cage (30 × 19 × 13 cm), with wood-chip bedding, a metal cage top, and a micro-isolator filter. For tissue collection, mice were anesthetized with 1.5% isoflurane (CAS 26675-46-7), and cervical dislocation was performed within approximately 5 min of induction. Retinas were immediately harvested for immunohistochemical analysis and total RNA sequencing. Although isoflurane can induce transcriptomic changes even after short exposure[31], it was selected to avoid retinal stress responses associated with other methods such as CO_2. Exposure time was minimized to reduce potential confounding effects.

Ethics declarations

The experimental research protocol on animals was approved by Chung-Ang University (approval no. 2020–00061) and followed the Animal Research Reporting of In Vivo Experiments (ARRIVE) guidelines[32]. All procedures were performed in compliance with relevant guidelines and regulations, as stated in the Methods section.

Immunohistochemistry

In brief, retinas from 5xFAD mice were rapidly excised by removing the lenses on a cold plate with phosphate-buffered saline (PBS). Retinal tissues were fixed in 4% paraformaldehyde (#15710; Electron Microscopy Sciences, Hatfield, PA, USA) for 1 h at 4 °C with gentle rotation, and subsequently incubated in 10%, 20%, and 30% sucrose-PBS solutions for 1, 3, and 12 h, respectively. The fixed retinas were embedded in either 7% agarose gel or OCT compound (4583, SAKURA, CA, USA), followed by sectioning with a vibratome (7000SMZ, Campden Instruments, England) or cryotome (CM1850, Leica, Germany), respectively. Following permeabilization in a solution of PBS containing 0.1% Triton X-100 for a duration of 10 min, the sections were subsequently blocked for 1 h in a solution consisting of 5% normal goat serum in PBS with 0.1% Triton X-100. Specimens were then incubated overnight at 4 °C with Aβ (1–42) primary antibodies (Cell Signaling, Danvers, USA), EGFLAM primary antibodies (PA5-31040, Invitrogen, USA), CtBP2 primary antibodies (612044, BD bioscience, USA), PKC-α primary antibodies (P4334, Santa Cruz Biotechnology, USA). After washing with PBS, specimens were incubated with secondary antibodies for 1 h at room temperature (23–25 °C) in the dark. Nuclear counterstaining was performed using 5 μg/ml 4′,6-diamidino-2-phenylindole (DAPI) for 3 min in the dark. Fluorescence images were captured using a Zeiss Axio Observer Z1 LSM 700 confocal microscope and processed with the ZEN program (ZEN lite 2011) (Carl Zeiss, Oberkochen, Germany). Confocal images were acquired from the superior central retina using identical acquisition settings. Aβ(1–42) signal intensity in the inner segment/outer segment (IS/OS) layer was quantified using ImageJ, based on the corresponding IS/OS region in each image.

Electroretinogram (ERG)

Mice underwent full-field flash electroretinography (ERG) to evaluate retinal function under scotopic and photopic conditions using the Espion e2 Visual Electrophysiology System (Diagnosys, Lowell, MA, USA). Briefly, for scotopic measurements, mice were dark-adapted overnight following anesthesia with 2X avertin solution (200 μL per 20 g mouse) containing tribromoethanol (T48402, SIGMA) and tert-amyl alcohol (240486; SIGMA). Prior to recording, pupil dilation was achieved using isoptoatropine (Alcon, Republic of Korea), followed by the

application of a small drop of 2% hypromellose (Samil, Republic of Korea) to each eye. Ground and reference subdermal electrodes were placed subcutaneously near the hindquarters and between the eyes, respectively, while the mice were positioned on a heated pad (37 ℃). ERG analysis was performed on five biological replicates per group (n = 5 for WT and n = 5 for 5xFAD) at each time point. Recording electrodes were then placed on the cornea, and ERG was conducted simultaneously under scotopic conditions for both eyes, using progressively increasing green light stimulus intensities. After a 2-min adaptation to 1.6 log cd s/m^2, photopic responses were recorded.

Total RNA isolation and reverse transcription-quantitative PCR (RT-qPCR)

Total RNA was extracted using TRIzol solution (15596018; Invitrogen, CA, USA) from approximately 100 mg of pooled retinal tissue (three retinas from three mice per group; n = 3 biological replicates), following the manufacturer's protocol. To remove any contaminated genomic DNA, 10 µg of total RNA was incubated with 20 units of RNase-free DNase I and 4 units of RNase inhibitor (both from New England Biolabs) in DEPC-treated water. The reaction mixture was incubated for 1 h at 37 °C, followed by 10 min at 60 °C. The RNA samples were then quantified spectrophotometrically at 260 nm, with an OD260:OD280 ratio ranging from 1.8 and 2.0, confirming their suitability for downstream analyses. cDNA synthesis was performed using Oligo-dT primers (6110A, Takara). 1 µg of total RNA was mixed with 1 µL of oligo-dT, and the mixture was preheated at 70 °C for 10 min to denature RNA secondary structures. The mixture was rapidly cooled to 4 °C, after which 2 µL of 10X reverse-transcriptase buffer, 10 mM DTT, 200 units of reverse transcriptase (18064022, Invitrogen, CA, USA) were added to reach a final volume of 20 µL. The reverse-transcription reaction was carried out at 40 °C for 60 min and terminated by heating at 94 °C for 20 s. The resulting cDNA was stored at −20 °C. Expression levels of mouse *Cngb1*, *Ppef2*, *Rpgrip1*, *Whrn*, *Prom1*, and *Crocc* mRNAs were assessed by RT-qPCR using specific primers listed in Supplementary Table 1. Primers were designed with Primer-BLAST and validated via a BLAST search in the NCBI database. The specificity of each amplified product was confirmed through melting curve analysis. Following the manufacturer's instructions, RT-qPCR was carried out using a Bio-Rad CFX96 Real-Time PCR Detection System using iQ SYBR Green PCR Supermix (#1708880, Bio-Rad, Hercules, CA, USA). The reference gene utilized for normalization was *Gapdh*, and the relative mRNA expression levels were computed using the $2^{-(\Delta\Delta Ct)}$ technique. All PCR reactions were conducted in duplicate for each experimental condition.

Library preparation and RNA-seq

The RNA-seq library was prepared using the TruSeq RNA Sample Preparation Kit v2 (Illumina, Inc., San Diego, CA, cat. no. RS-122–2002). Briefly, 100 ng of total RNA from each sample was utilized. Poly-A mRNA was isolated by binding to poly-T oligo-attached magnetic beads, followed by mRNA fragmentation. The cleaved RNA fragments were then reverse transcribed into double-stranded cDNA. Following the degradation of the RNA template, a random primer with an Illumina-compatible linker sequence at the 5′ end was used to start second-strand synthesis. The resulting double-stranded cDNA library was purified with AMPure XP beads (A63881; Beckman Coulter, CA, USA) to remove all reaction components. The library was then amplified to add complete adapter sequences necessary for cluster generation, followed by another round of purification to remove PCR components. The quality and size distribution of the libraries were evaluated using an Agilent 2100 Bioanalyzer equipped with a High-Sensitivity DNA Chip (Agilent Technologies, Santa Clara, CA) Finally, the cDNA libraries were sequenced using paired-end 75 sequencing on an Illumina NextSeq 500 system (Illumina, Inc., San Diego, CA).

Bioinformatical analysis for RNA-seq

mRNA-seq data quality was assessed using FastQC (v.0.11.9). The low quality and TruSeq adapter sequence in mRNA-seq reads were trimmed using TrimGalore (v.0.6.6). Indices were generated from the GRCm38.p6.101 genome assembly sequence to align the representative transcript sequences to both the genome and transcriptome. The alignment of sequences to the reference genome was performed using STAR (v.2.7.1a) with the ENCODE v3 parameters. Alignment sequences were applied for transcript assembly and estimation of their abundances using RSEM (v.1.3.3). The statistics for differentially expressed transcripts (or genes) and fragments per kilobase of transcripts per million mapped reads (FPKM) were calculated using DESeq2 (v.1.32.0).

Identification of differential RI events

To detect and quantify RI events in all known introns, rMATS (v.4.1.2), IRFinder (v.1.3.0), and iREAD (v.0.8.9) were used. The analysis involved performing rMATS on trimmed FASTQ files with default parameters, and the resulting junction and exon counts were used for RI detection. IRFinder was performed from trimmed FASTQ with default parameters. Differentially expressed RI events were calculated using a generalized linear model in DESeq2. In the case of iREAD, bam files generated from the STAR aligner were used with the ENCODE v3 parameter. The read count output from iREAD was used as an input to DESeq2 for detecting RI events.

Statistical analysis

All results are expressed as mean ± standard error of the mean (SEM). Statistical comparisons between groups were performed using unpaired two-tailed Student's *t*-test, using GraphPad Prism version 5.01 (GraphPad Software, CA, USA). A P-value of less than 0.05 was considered statistically significant.

Results

Profiling of transcriptomic dynamics in the retinas of 5xFAD mice

In certain cases of AD, Aβ was found to be deposited in entire retinal layers, encompassing the outer nuclear, outer plexiform, inner nuclear, inner plexiform, and ganglion cell layers. Consistently, we detected the accumulation of

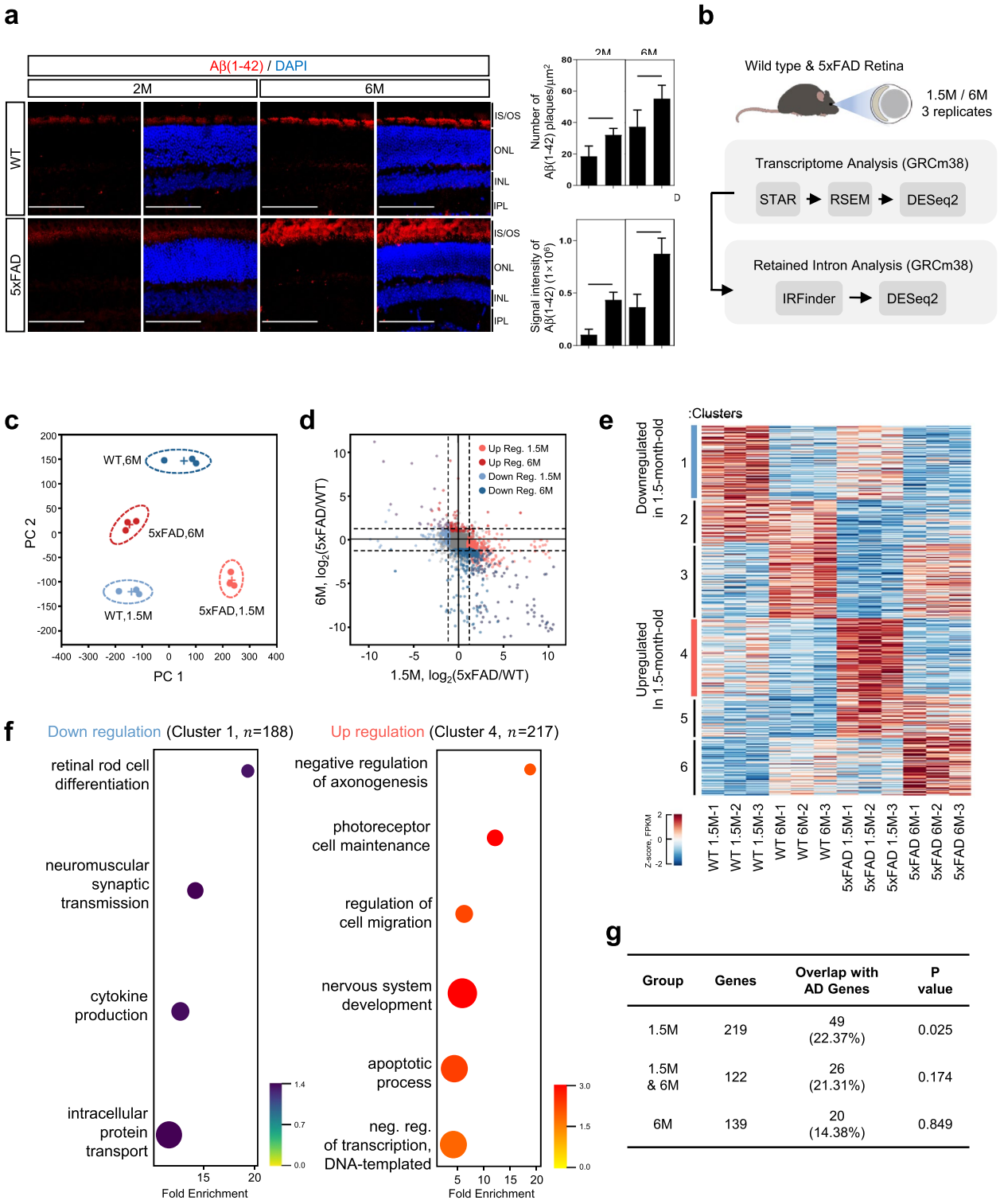

g

Group	Genes	Overlap with AD Genes	P value
1.5M	219	49 (22.37%)	0.025
1.5M & 6M	122	26 (21.31%)	0.174
6M	139	20 (14.38%)	0.849

Aβ plaques in both 2- and 6-month-old 5xFAD mouse retinas (Fig. 1A). The number and signal intensity of Aβ plaques in inner and outer segments (IS/OS) were significantly higher in 2-month-old 5xFAD than in wild type (WT) mouse retinas (Fig. 1A). In 5xFAD brain tissues, aging was associated with a global increase in Aβ plaques (supplementary Fig. S1A–C).

To identify differentially expressed genes (DEGs) in 5xFAD mouse retinas, RNA-seq analysis was conducted on 1.5-month-old mice to examine early onset AD-like amyloidosis and on 6-month-old mice to assess AD-like amyloidosis progression (Fig. 1B)[33]. Principal component analysis was employed to validate the most substantial variances among groups and to ensure reproducibility among biological replicates (Fig. 1C, supplementary Fig. S1D). The volcano plots depict the statistical significance and corresponding expression levels of differentially expressed transcripts (DETs) under each experimental condition (DESeq2 P-value < 0.05, absolute log2 fold change abs ($\log_2$FC) ≥ 1 and variance-to-mean ratio ≤ 1) (supplementary Fig. S1E). Compared with the retinas of

◀**Fig. 1**. Analysis of transcriptome dynamics in the retina of 5xFAD mice. (**A**) Immunofluorescent confocal images of amyloid-β (red), 4′,6-diamidino-2-phenylindole (DAPI) (Blue)-stained retina of 2- and 6- month-old wild type (WT) and 5xFAD mice. Images were taken from the superior retina. Scale bar = 50 µm. Aβ plaques are mainly localized to the IS/OS layer. Right: Quantification of Aβ(1–42) plaque number and signal intensity per field of view. Specifically, the number of amyloid plaques was measured per μm^2, and plaque signal intensity was quantified per 4 μm^2 area in 15 µm-thick coronal sections at the level of the outer segment (OS), using ImageJ software. Quantification was performed in both 2- and 6-month-old WT and 5xFAD mice. Data represent mean ± SEM. Statistical analysis: unpaired two-tailed Student's t-test (****$P < 0.0001$). (**B**) Experimental design and transcriptome analysis pipeline. (**C**) Principal component analysis (PCA) of RNA-seq data from male hemizygous 5xFAD and age-matched WT mice (n = 3 biological replicates per group). (**D**) Scatter plot illustrating transcript expression pattern changes in 1.5-month and 6-month 5xFAD mice relative to WT controls. Upregulated transcripts are highlighted in pink (1.5-month-old) and red (6-month-old), while downregulated transcripts are highlighted in light blue (1.5-month-old) and blue (6-month-old). Filtering criteria used: ($abs(log_2FC) > 1.0$, P-value < 0.05 VMR ≤ 1) in each 1.5- and 6-month group. (**E**) Clustering of transcripts using k-means clustering from differentially expressed transcripts (a total of 7020 transcripts). Upregulated transcripts are highlighted in red (cluster 4), while downregulated transcripts are highlighted in blue (cluster 1) in the 1.5-month-old group only. (**F**) Gene Ontology (GO) terms of biological process analysis in cluster 1 and cluster 4. (**G**) Overlap of DETs in 5xFAD groups with curated AD genes from DisGeNet. Statistical significance was assessed using a two-tailed chi-square test with Yates's continuity correction. *AD* Alzheimer's disease, *DETs* differentially expressed transcripts.

1.5-month-old WT mice, the retinas of 1.5-month-old 5xFAD mice exhibited 2566 upregulated transcripts and 1331 downregulated transcripts (supplementary Fig. S1F, left). In 6-month-old mice, the DET analysis revealed 1108 upregulated transcripts and 2,015 downregulated transcripts (supplementary Fig. S1F, right). In Fig. 1D, we visualized the differential expression trends of transcripts between 1.5- and 6-month-old 5xFAD mice using a bivariate scatter plot. Each dot represents a transcript, with its x-axis value indicating the log_2 fold-change between 1.5 M 5xFAD and WT, and the y-axis value showing the same comparison at 6 M. Transcripts located in the same quadrant are consistently regulated, while those in opposite quadrants exhibit reversed expression trends between the two time points.

We then applied k-means clustering (k = 6) to DETs, with the value determined using the elbow method (supplementary Fig. S1G). A heatmap was generated to visualize the expression patterns of the six clusters identified using k-means clustering (Fig. 1E, supplementary Fig. S1G). Given the observed structural abnormalities and visual dysfunction in the early stages of 5xFAD mouse retinas[21,22], we focused on clusters 1 and 4, which were specifically down- or upregulated in the retinas of 1.5-month-old 5xFAD mice. To identify transcriptomic pathways relevant to the 1.5-month-old group, gene ontology (GO) analysis was conducted on upregulated (n = 217) and downregulated (n = 188) genes. The upregulated DEGs were categorized into several functional groups, including "negative regulation of axonogenesis", "photoreceptor cell maintenance", "nervous system development", and "apoptotic process" (Fig. 1F, left panel). GO of downregulated DEGs was classified as "retinal rod cell differentiation" and "neuromuscular synaptic transmission" (Fig. 1F, right panel). Interestingly, 22% of the upregulated genes in cluster 4 were found to overlap with the curated AD gene list from the Disease Gene Network (DisGeNet) database[34] (P-value < 0.05, two-tailed χ^2 test with Yates' correction) (Fig. 1G).

Previous studies have raised concerns about early retinal changes in 5xFAD mice due to the potential influence of retinal degeneration-associated alleles, such as *Pde6b* and *Trem2*[35–37]. To address this, we performed sequencing analysis of $Pde6b^{rd1}$ and $Trem2^{S148E}$ —genes implicated in retinal degeneration—at 1.5 and 6 months of age in both WT and 5xFAD mice. Additionally, we examined other relevant alleles, including *Prph2* and *Rd3*. Our results confirmed that both control (C57BL/6 J WT) and 5xFAD mice do not carry any mutations in these retinal degeneration-associated alleles (supplementary Fig. S2).

These findings suggest that the gene expression changes observed in the early stages of 5xFAD may be related to the maintenance of retinal function and cell death. Furthermore, the altered gene expression patterns in the 5xFAD retina show a significant correlation with genes associated with Alzheimer's disease in the retina.

Dysregulation of AS in the retina of 5xFAD mice

As we previously found that changes in the cellular microenvironment can affect the splicing function in the cytotoxic responses and diseased tissues[38], the cytotoxic effect of Aβ plaque in AS events was analyzed. To examine AS events in the retinas of 5xFAD mice, rMATS[39] was applied to identify splice site variants. Considering the retinas of 1.5-month-old 5xFAD mice, statistically significant (P-value < 0.05) splice site variants in protein-coding genes were as follows: skipped exons (SE), 2100 genes; RI, 745 genes; an alternative 5′-splice site (A5SS), 388 genes; an alternative 3′-splice site (A3SS), 588 genes; and mutually exclusive exons (MXE), 210 genes. Considering the retinas of the 6-month-old 5xFAD mice, significant splice site variants were as follows: SE, 2,496 genes; RI, 831 genes; A5SS, 428 genes; A3SS, 678 genes; and MXE, 446 genes (Fig. 2A). Given the presence of increased RI during aging and in AD brain tissues[12], we analyzed and compared RI in mouse retinas using three algorithms: IRFinder[40], iREAD[41], and rMATS. IRFinder calculates an RI ratio of intronic and exonic abundance to identify RI events. iREAD introduces the Shannon entropy score to measure the uniformity of the distribution patterns of mapped reads in RI regions. rMATS focuses on uniquely mapping read-in splice sites and uses Bayesian statistical frameworks. In the retina of 1.5-month-old 5xFAD mice, IRFinder detected 2960 statistically significant events (P-value < 0.05), whereas iREAD identified 489 events. In the retina of 6-month-old 5xFAD mice, 3871 and 423 events were detected using IRFinder and iREAD, respectively (Fig. 2B). IRFinder

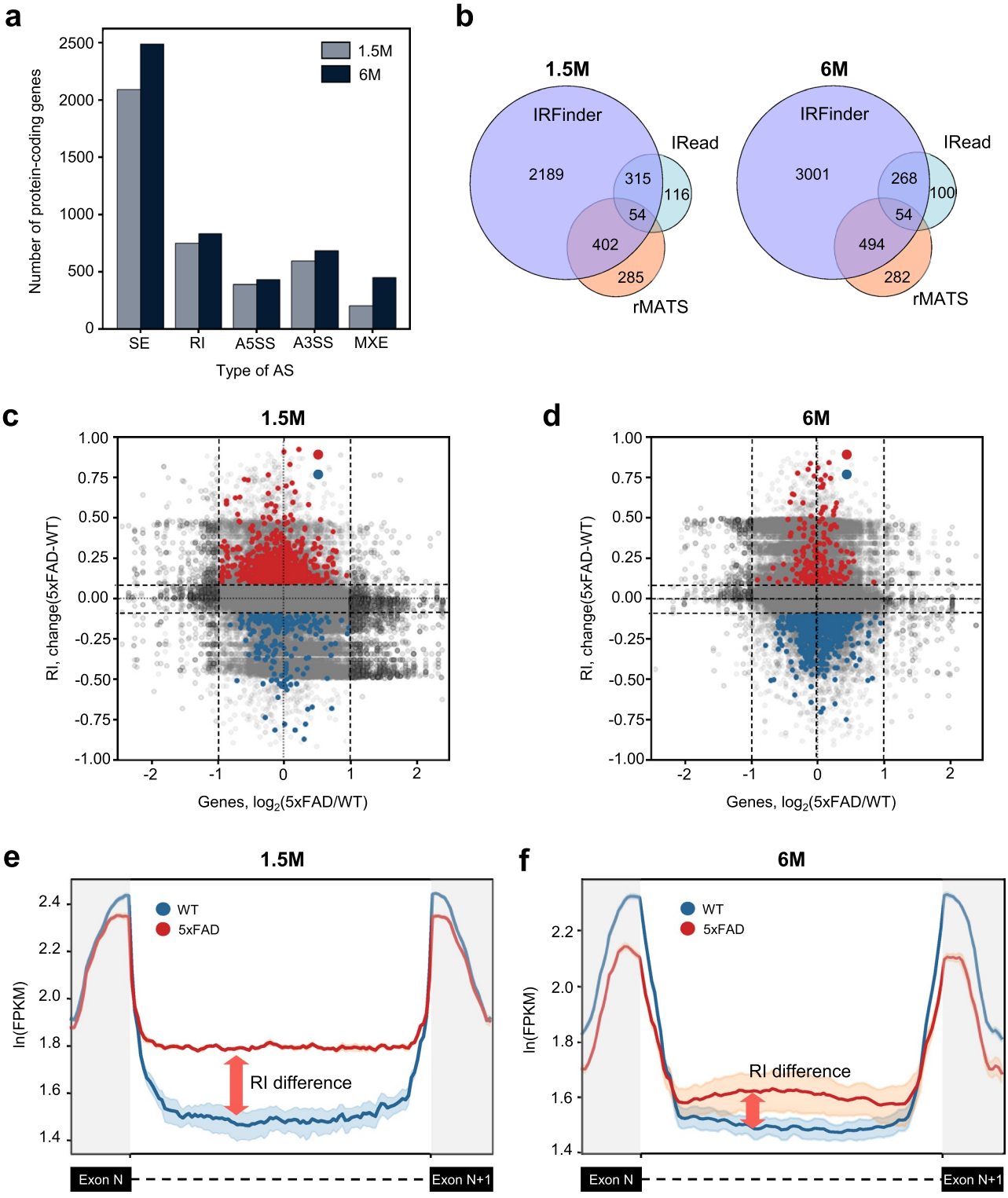

Fig. 2. Differential RI mark in 5xFAD mouse retinas. (**A**) Alternative splicing events in protein-coding genes were assessed using the rMATS (P-value < 0.05) for 1.5-month (blue) and 6-month (orange) old mice. (**B**) Venn diagram illustrating the significant RI events using IRFinder, iREAD, and rMATS in 1.5- and 6-month-old mice. (**C**, **D**) Scatter plots represent the difference of RI ratio in relation to log2 fold-change of gene expression for (**C**) of 1.5-month and (**D**) 6-month-old mice. Upregulated and downregulated RI events with strict filtering criteria (difference of RI ratio > 0.1, P-value of RI < 0.05) in non-regulated genes (log2FC < 1 and P-value > 0.05) are represented by red dots and blue dots, respectively. (**E**, **F**) Profile plots showing the upregulated (upper panel) and downregulated (lower panel) RI regions in (**E**) 1.5-month-old and (**F**) 6-month-old mice.

was used in the following analysis because it not only verified statistically significant RI events but also detected overlapped events using other algorithms.

To identify only the RI effect, we focused on RI events in genes that showed non-significantly different expressions between WT and 5xFAD mouse retinas. Intron-retaining transcripts have lower expression levels owing to nonsense-mediated mRNA decay, which directly impacts the detectability of RI[42]. Therefore, we analyzed RI events identified in protein-coding genes that exhibited no differences in the mRNA expression level. The differential RI was extracted through DESeq2 P-value < 0.05 and the difference of the RI ratio over 0.1 between the 1.5-month-old WT and 5xFAD mouse retinas (Fig. 2C). Upon performing a pairwise comparison between the retinas of 5xFAD and WT mice, we identified 766 upregulated and 210 downregulated RI events in 5xFAD mice (Fig. 2C). The same conditions were applied to the 6-month-old group to identify differential RI, yielding 208 and 741 RI events in the retinas of 5xFAD mice and WT mice, respectively (Fig. 2D). FPKM of RI-enriched regions was significantly increased in the retina of 1.5-month-old 5xFAD mice than in WT mouse retinas when FPKM exon regions showed similar expression in both groups (Fig. 2E). The profile plots of RI-enriched regions in 6-month-old 5xFAD mouse retina showed similar patterns (Fig. 2F). Interestingly, the RI-enriched region in the 1.5-month-old group showed a more significant difference between groups and lower variance in replicates than those in the 6-month-old group. Taken together, AS events were identified in the early stages of 5xFAD mouse retinas, with notable and significant changes observed in RIs.

Increased RI events in 5xFAD mouse retina

We next attempted to identify specific genes in 5xFAD where RI can be prominently detected by performing additional analyses. Applying the criteria of FPKM > 1.0 in the RI region and variance-to-mean ratio < 1 across all groups, we acquired differentially enriched RIs. A total of 613 differentially RI-enriched regions were identified in the 1.5-month-old 5xFAD mouse retina, while 607 RI regions were identified in the 6-month-old 5xFAD mouse retina. Next, differentially expressed RI regions for each group were identified through the application of *k*-means algorithms (with k = 2), revealing 543 RI-enriched regions in the retina of 1.5-month-old 5xFAD mice (Fig. 3A). The same algorithm was applied to identify 75 specific RI-enriched regions in 6-month-old 5xFAD mouse retina (Fig. 3B). To further assess the functional importance of RI-enriched genes, we conducted the GO analysis. The genes of 5xFAD-specific RI regions in 1.5-month-old mice (n = 362) were involved in "photoreceptor cell maintenance", "visual perception", "cell projection organization," and "DNA repair" (Fig. 3C), while "ubiquitin-dependent protein catabolic process" and "protein deubiquitination" were enriched in the retina of 6-month-old 5xFAD mice (supplementary Fig. S3A). We observed an overlap of 22% between upregulated genes and curated AD genes in 1.5-month-old 5xFAD mice, as described in Fig. 1G. Consistently, our results further revealed that approximately 18 and 19% of differential RI genes in the retinas of 1.5- and 6-month-old 5xFAD mice overlapped with curated AD genes (supplementary Fig. S3B), respectively. Notably, these differential RI genes demonstrated significant overlap with retinal marker genes, accounting for 32.81 and 39% in the retinas of 1.5- and 6-month-old 5xFAD mice, respectively (supplementary Fig. S3B).

All RI regions and mRNA expressions are visualized using a circos plot to substantiate the presence of RI patterns in the retinas of 1.5-month-old 5xFAD mice (Fig. 3D). The outmost circle displayed a scatter depicting log10 (-P values) of significantly upregulated RI in the retina of 1.5-month-old mice. The second and third circles represent the expression of all protein-coding genes as log2 scale. The last circle shows retinal marker genes associated with crucial retinal functions, including retinal homeostasis, retinal development, and visual perception. A subset of RI events persisted within genes related to retinal functions, including *Rpgrip1*, *Pde6b*, *Gnb1*, and *Cacna1f*. These findings emphasize the occurrence of RI in early-stage 5xFAD mouse retinas, particularly in genes associated with retinal markers, including those involved in functional homeostasis.

Effects of RIs of the retina of 5xFAD mice in physiological impairment

To validate whether retained introns (RIs) were enriched in retinal marker genes (*Rpgrip1*, *Whrn*, *Prom1*, *Crocc*, *Cngb1*, and *Ppef2*) in early-stage 5xFAD mouse retinas, we performed qPCR using primer pairs designed to target exon–intron junctions within the RI regions (Fig. 4). Integrated Genome View (IGV) tracks visualized RI signal in WT (blue) and 5xFAD (red) retinas at 1.5 months of age, with reduced read coverage at intronic regions suggesting partial retention. Consistent with RNA-seq findings, RT-qPCR confirmed significantly increased RI levels in all six genes in 5xFAD retinas. These results support early dysregulation of splicing and transcript processing in photoreceptor-related genes during AD-associated retinal degeneration.

To determine the physiological dysfunction of phototransduction by RI events, we analyzed the ERGs of 1.5- and 6-month-old WT and 5xFAD mice under both dark-adapted (scotopic) and light-adapted (photopic) conditions. The magnitude of the scotopic ERG a-wave and b-wave corresponded to processes involving phototransduction in the OS of rod cells and the synaptic transmission between rod spherules and rod bipolar cells. In 1.5-month-old 5xFAD mice, scotopic ERG amplitudes were significantly reduced compared with WT mice (Fig. 5A). Specifically, a-wave responses were decreased at mid-to-high stimulus intensities (54.70 ± 5.374 versus 28.37 ± 1.767 μV at 0.7 log cd s/m^2, P-value = 0.0331 / 48.05 ± 2.475 versus 25.22 ± 7.665 μV at 1.0 log cd s/m^2, P-value = 0.0035), indicating impaired rod phototransduction. Additionally, b-wave amplitudes were significantly lower in 5xFAD mice across multiple intensities (169.4 ± 18.88 versus 98.23 ± 20.39 μV at 0.7 log cd s/m^2, P-value = 0.0296), reflecting possible dysfunction in rod-to-bipolar cell signaling (Fig. 5A, supplementary Fig. S4A, left). In contrast, photopic ERGs at 1.5 months showed no significant differences in either a- or b-wave amplitudes between genotypes, suggesting that cone pathway function was relatively preserved at this stage (Fig. 5B, supplementary Fig. S4A, right). By 6 months of age, 5xFAD mice continued to exhibit reduced scotopic a- and b-wave responses compared to WT, although the degree of reduction was milder than at 1.5 months. This may reflect partial adaptation or compensation over time, or differential vulnerability of retinal circuits (Supplementary Fig. S4B, left). Notably, photopic responses remained largely comparable between WT and

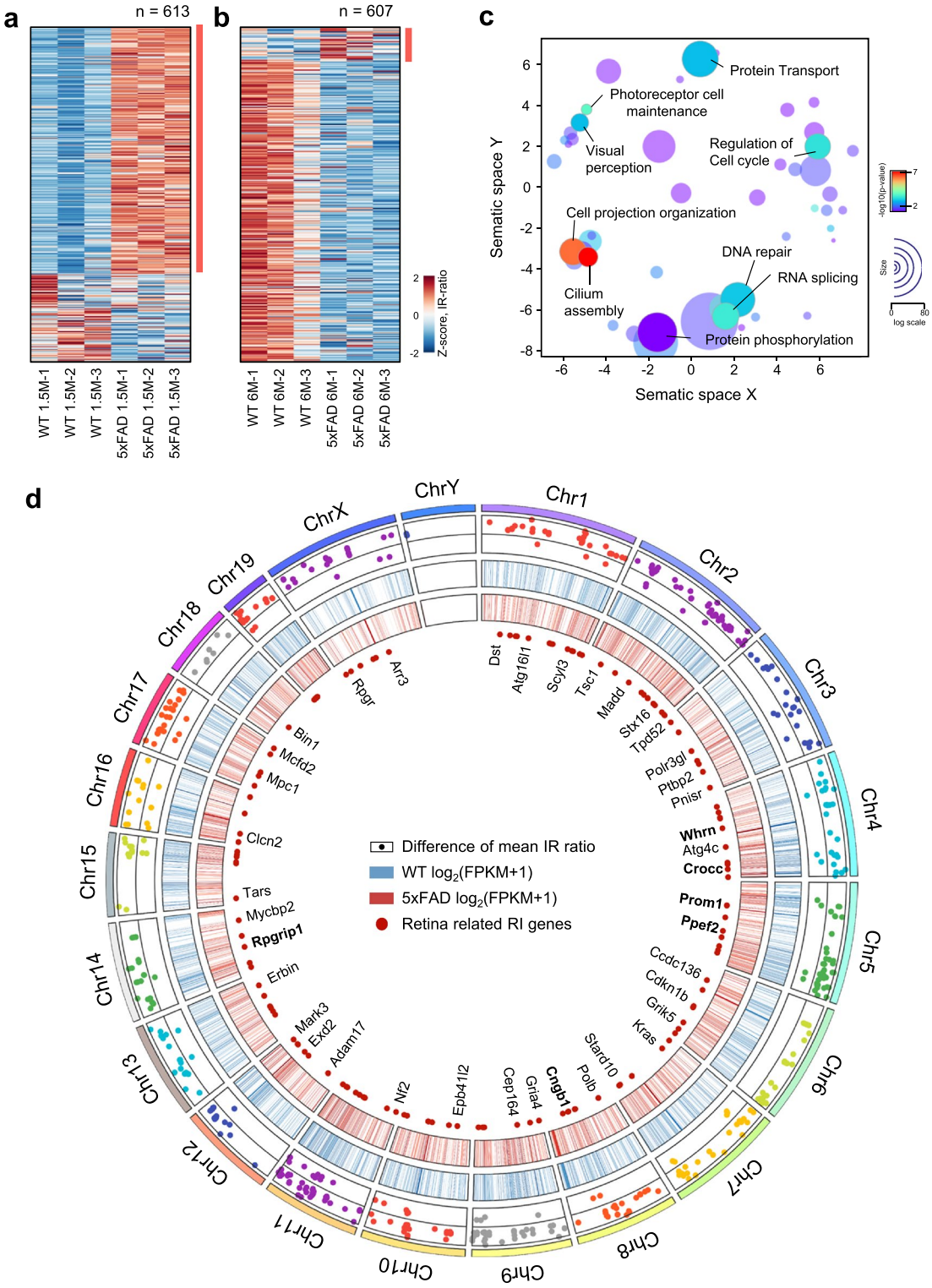

Fig. 3. Analysis dynamics of RI patterns in 5xFAD mouse retina. (**A**, **B**) Clustered heatmap of (**A**) 613 RIs in the retinas of 1.5-month-old and (**B**) 607 RIs in 6-month-old mice using k-means method. (**C**) The scatter plot illustrates confidence scores for enriched gene ontologies associated with clustering based on functional similarity in the semantic space. Gene Ontology (GO) analysis of biological processes was performed using the DAVID tool, highlighting upregulated regulatory interactions (RIs) in 1.5-month-old mice (362 genes in 543 events). (**D**) Circos plot displaying integrated transcriptomic and retained intron (RI) dynamics in the retina of 1.5-month-old 5xFAD mice. The outer ring represents log10 (-P values) of significantly upregulated RI events. The second and third rings show the expression levels of all protein-coding genes in WT (blue) and 5xFAD (red) retinas, respectively. The innermost ring illustrates differences in mean RI ratios between WT and 5xFAD mice. Retinal marker genes associated with key retinal functions, including retinal homeostasis, are indicated as red dots. Genes of particular interest, highlighted as candidate early biomarkers, are shown in bold.

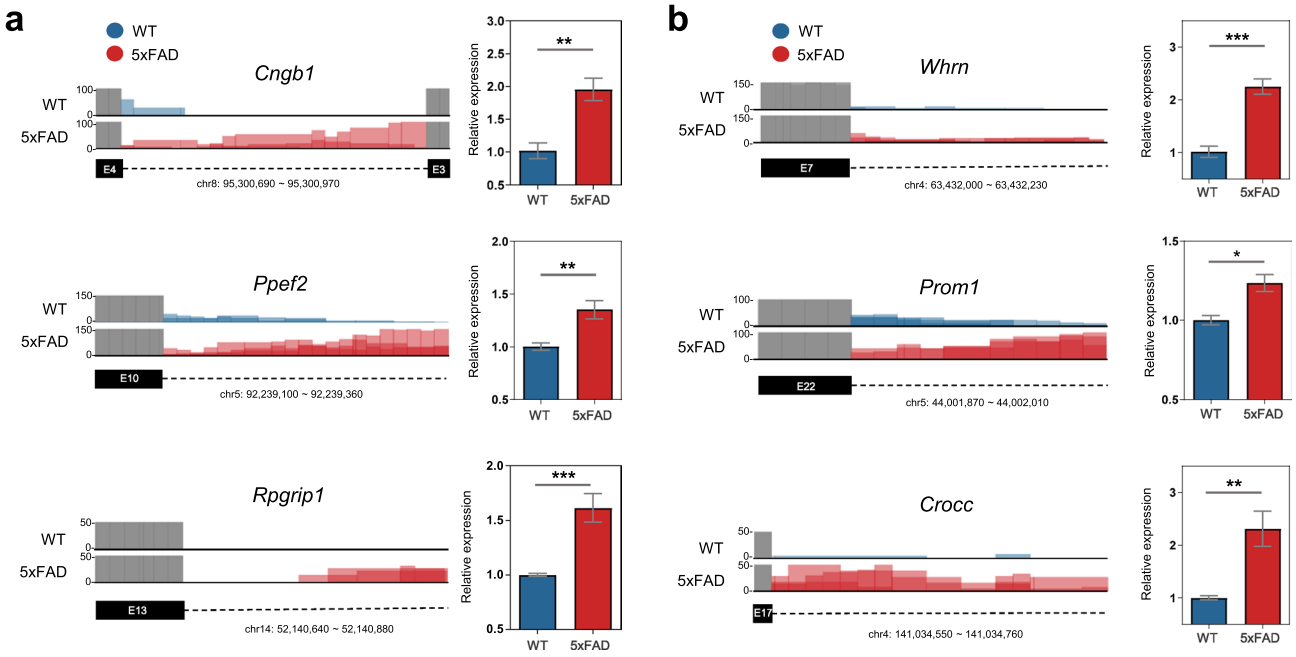

Fig. 4. Experimental validation of RI at retinal marker genes in 5xFAD mouse retina. (**A**, **B**) Integrated Genome Viewer (IGV) tracks (left) and RT-qPCR results (right) for RI levels in six retinal marker genes. (**A**) *Rpgrip1*, *Whrn*, *Prom1*, and *Crocc* were selected from the non-DEG RI set used in Fig. 3D. (**B**) *Cngb1* and *Ppef2* were identified from DEG-associated RIs. IGV tracks show read coverage in WT (blue) and 5xFAD (red) retinas at 1.5-month-old mice. RT-qPCR was performed using exon–intron junction primers. Each RNA sample was pooled from one retina per mouse across three male mice (n = 3 per group). Data represent mean ± SEM. Unpaired two-tailed Student's t-test was used for statistical analysis (*P < 0.05, **P < 0.01, ***P < 0.001).

5xFAD mice at 6 months, consistent with selective early impairment of rod-mediated pathways (Supplementary Fig. S4B, right). In addition, there was no significant alteration in the implicit time of a- and b-waves between the 5xFAD and control conditions (supplementary Fig. S4C).

To further assess whether RI-associated transcriptomic changes result in altered protein expression, we performed IHC for retinal cell markers, EGFLAM (photoreceptor ribbon synapses), CABP2 (cone bipolar cells), and PKCα (rod bipolar cells), in 1.5-month-old 5xFAD and WT retinas (Supplementary Fig. S5). Consistent with the ERG findings, EGFLAM and CABP2 signal intensities were significantly reduced in the outer plexiform layer (OPL) of 5xFAD mice, indicating structural and functional disruption at photoreceptor-to-bipolar cell synapses (Supplementary Fig. S5A,B). In contrast, PKCα levels remained unchanged, suggesting relative preservation of rod bipolar cell bodies at this stage (Supplementary Fig. S5C). These protein-level alterations provide indirect support for the hypothesis that RI accumulation impairs phototransduction and synaptic function in early-stage 5xFAD retinas. Taken together, these findings indicate that deficits in rod phototransduction and downstream signaling emerge as early as 1.5-month-old in 5xFAD mice, potentially driven by early RI accumulation and mis-splicing of photoreceptor-specific transcripts.

Discussion

With the rising global incidence of AD, largely driven by the aging population, extensive efforts have been dedicated to devising effective methods for screening high-risk individuals before the onset of AD symptoms or detecting AD in its early stages. In recent decades, substantial advancements have been made in comprehending the pathophysiology of AD and formulating intervention approaches. Nonetheless, there remains a lack of effective treatments and sufficient diagnostic tools for AD. Therefore, there is an urgent need for biomarkers for AD to enable early diagnosis and risk assessment for this condition.

In the last decade, our comprehension of AD has expanded substantially beyond its well-established definitive indicators, namely cerebral Aβ plaques and neurofibrillary tangles. The presence of Aβ accumulation in the brain has been extensively documented, while the identification of these specific biomarkers in the retina has only recently been detected. In 2008, Ning and collaborators were the pioneers in demonstrating that the accumulation of Aβ in the 5xFAD mouse retina was linked to neurodegeneration[43]. Among various AD-related mouse models, we employed 5xFAD mice, well known for their early onset and the initiation of amyloid plaque formations. Our observations distinctly revealed the presence of AD in the retina, hippocampus, and cerebral cortex between 1.5 and 6 months of age (Fig. 1A and supplementary Fig. S1A,B). The retina functions as the primary sensory organ for vision and plays a crucial role within the central nervous system. The retina is regarded as an extension of the brain and a potential biomarker for AD. Recently, retinal biomarkers for the

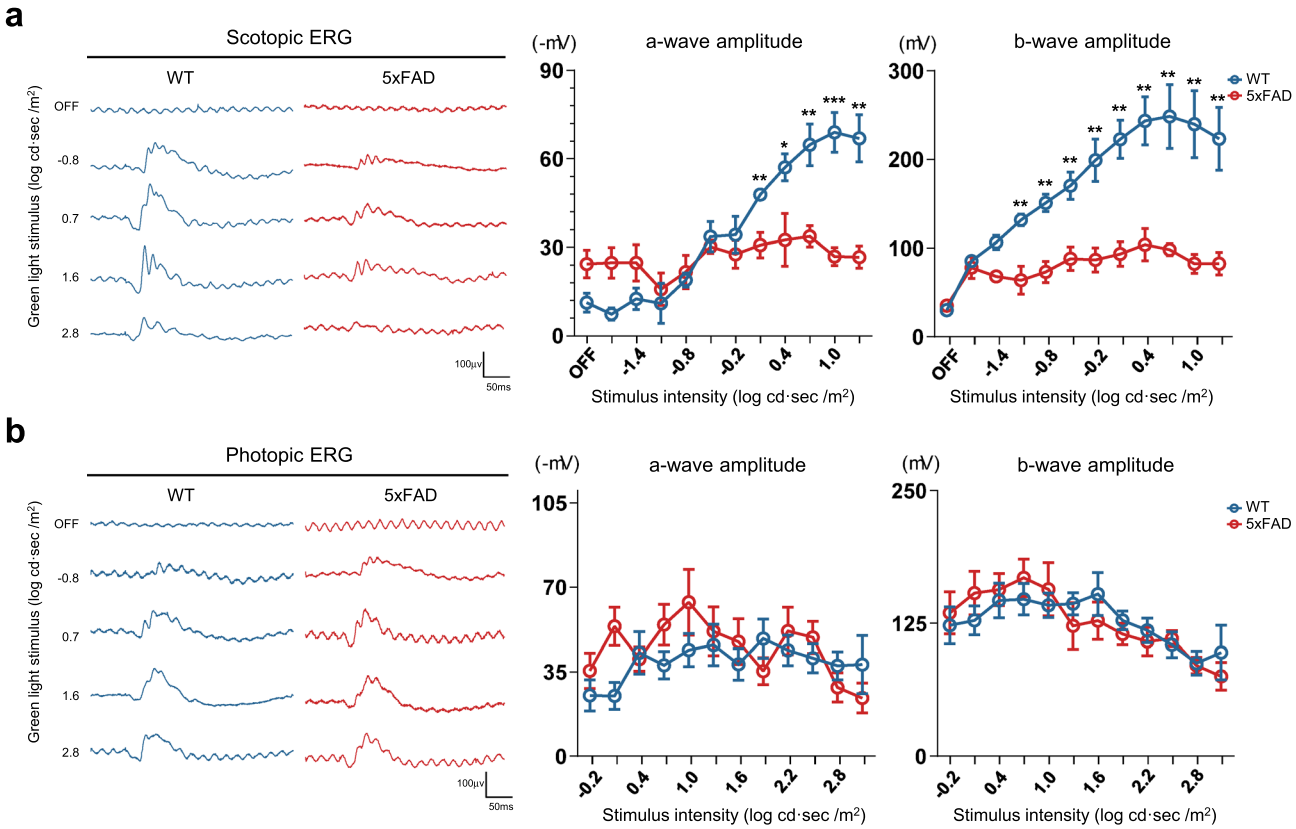

Fig. 5. Early detection of physiological changes in 5xFAD mouse retina using electroretinogram (ERG). (**A**) Representative scotopic ERG traces recorded from 1.5-month-old WT (n = 5) and 5xFAD (n = 5) hemizygous mice under five green light stimuli (OFF, − 0.8, 0.7, 1.6, and 2.8 log cd s/m^2). Right: a-wave and b-wave amplitudes plotted against stimulus intensity (− 1.7 to 1.3 log cd s/m^2). (**B**) Representative photopic ERG traces under the same stimulus conditions. Right: a-wave and b-wave amplitudes across − 0.2 to 3.1 log cd s/m^2. Data are presented as mean ± SEM. Sample sizes: WT (n = 5), 5xFAD (n = 5). Error bars are shown for all points. Statistical significance was assessed using unpaired two-tailed Student's t-test at each intensity. (*P < 0.05, **P < 0.01, ***P < 0.001).

early detection of patients at high risk of AD have been discovered[44–47]. Considering that the retina serves as a "window" to the brain and offers a valuable avenue for exploring AD pathophysiology, the examination of retinal changes holds considerable potential in the early detection of AD[48]. However, precise mechanisms underlying the pathophysiology and alteration of gene expressions in AD remain poorly understood.

AS is a critical factor influencing the transcriptome complexity in the AD transgenic mouse (5xFAD). Notably, AS governs a distinct group of genes that are differentially regulated at the transcriptional level. Consequently, AS is an additional and highly adaptable mechanism for understanding proper regulation of gene expression. Our research has identified elevated RI as a crucial result of dysregulated splicing in the context of aging and AD pathogenesis in the retina. Changes in splicing and RI at specific genes during aging may underlie AD progression from a normal state to different stages of AD. To investigate this hypothesis, it is crucial to analyze the RI patterns derived from the retina of WT mice (1.5- and 6- months) and mice with mild cognitive impairment and advanced stages of AD (1.5- and 6- months of 5xFAD) using RNA-seq data. In the present study, we clearly demonstrated that RI occurs during the pre-disease state in the retina when pathological alterations could be observed in the brain (Fig. 2). Supporting this, recent transcriptomic studies have shown that aberrant splicing, including RI, is a common feature in AD-affected brain regions. For instance, Liang et al. (2024) reported elevated RI of the DDIT4L gene in the hippocampal dentate gyrus of AD model mice, where the intron-retaining isoform colocalized with Aβ plaques and contributed to synaptic dysfunction[49]. While these findings suggest that RI is not exclusive to the retina, our data highlights that such events arise considerably earlier in the retina than in classical brain regions like the hippocampus. This implies that the retina may serve as a sensitive sentinel tissue for early post-transcriptional dysregulation in AD. Its accessibility and development ties to the CNS further underscore its utility as a non-invasive site for biomarker discovery. Future comparative studies across CNS regions, including the hippocampus, cortex, and retina, are warranted to determine whether RI represents a shared or tissue-specific feature in early AD progression, and to validate RI-based retinal biomarkers for early diagnosis and monitoring.

Building on this, examining quantitative changes in transcription patterns during disease could reveal new candidate biomarkers for neurodegenerative diseases. Here, we observed the augmentation of the RI in six particular genes within the retina of 1.5-month-old 5xFAD mice. Among them, *Cngb1*, *Ppef2*, and *Rpgrip1* are known to be involved in the phototransduction process and are crucial for the viability and functionality of photoreceptor cells. *Cngb1* is a subunit of the cGMP-gated channel found in rod photoreceptors. Its primary function is to regulate the flow of ions into the OS of rod photoreceptors in response to light-induced changes in intracellular cGMP levels[50,51]. *Ppef2* encodes a photoreceptor protein that also plays a role in rod phototransduction and dephosphorylates photoactivated rhodopsin[52]. *Rpgrip1* encoded protein interacts with GTPase regulator protein and is a key component of cone and rod photoreceptors. *Rpgrip1* is required for normal disk morphogenesis and disk organization in the OS of photoreceptor cells and for survival of photoreceptor cells[53–55]. Furthermore, *Whrn*, *Prom1,* and *Crocc* are involved in the maintenance of the cilium of photoreceptors that include the periciliary membrane complex, ciliogenesis, and key regulators of disk morphogenesis[46,56,57].

ERG assesses the function of retinal cells by exposing the eye to light stimuli and measuring the resulting electrical responses. In 6-month-old 5xFAD mice, amyloid plaques had expanded across the hippocampus and neocortical areas, with spatial learning deficits becoming apparent around 4 months of age[33,58]; synapse degeneration, dysfunction, and neuronal loss were also observed in the hippocampus by approximately 6 months[59]. Interestingly, we observed that ERG responses in 1.5-month-old 5xFAD mice were already significantly reduced under scotopic conditions, indicating early rod photoreceptor dysfunction (Fig. 5). However, we recognize that the interpretation of these early ERG deficits must be made with caution. Previous report has shown preserved a-wave amplitudes in 6-month-old 5xFAD mice[60], suggesting that rod photoreceptor responses may remain relatively intact at later stages. Therefore, the greater reduction in b-wave amplitude observed here may reflect early synaptic alterations, such as dysfunction of rod bipolar cells, rather than primary rod degeneration. Moreover, technical and biological factors, including our limited sample size and the exclusive use of male mice, may have contributed to variability in ERG responses.

In support of the early functional impairments observed by ERG, we also detected protein-level alterations using immunohistochemistry. Although we did not assess the RI-target genes directly due to technical limitations, signal intensities of EGFLAM and CABP2—markers of photoreceptor synapses and cone bipolar cells, respectively—were significantly reduced in 5xFAD retinas. These changes, localized to OPL, are indicative of synaptic disruption and align with the hypothesis that aberrant splicing events, such as RI, may lead to reduced protein output. In contrast, PKCα levels remained stable, suggesting that not all retinal cell types are equally vulnerable at this early stage. While these findings do not provide direct proteomic validation of RI targets, they offer functional support for the idea that splicing dysregulation can precede or accompany synaptic failure in the AD retina (Supplementary Fig. S5).

Comprehensive transcriptomic and physiological analyses suggest that aberrant intron retention (RI) in photoreceptor-related genes contributes to these early ERG deficits. These findings highlight the potential of ERG as a non-invasive and quantifiable early biomarker for AD. Notably, RI changes were more prominent at 1.5 months than at 6 months, despite a lower Aβ burden at the earlier time point. This seemingly paradoxical observation aligns with one of the central aims of our study: to uncover splicing-specific dysregulation independent of gene expression changes. By focusing on RI events in non-differentially expressed genes (non-DEGs), we were able to detect early splicing alterations without confounding effects from global transcriptional dysregulation. Although RI changes in non-DEGs were more distinct at 1.5 months, this does not suggest a reduced overall RI burden at 6 months. In fact, when the DEG filter was removed and a relaxed statistical threshold was applied (RI ratio > 0.1, $P < 0.05$), the total number of RI events was higher at 6 months than at 1.5 months (2441 vs. 2,371; Fig. 2A,B). However, extensive gene expression changes at this later stage make it difficult to attribute RI events specifically to splicing defects. Thus, the clearer RI patterns observed at 1.5 months likely represent early-stage, splicing-specific abnormalities that precede widespread transcriptional shifts and Aβ pathology. This supports the notion that the retina undergoes early molecular perturbations in AD, and that RI may serve as a sensitive and specific biomarker for detecting preclinical retinal involvement. While these findings support the potential of RI as an early AD biomarker, one limitation of our RNA-seq analysis lies in the statistical threshold used during RI filtering. Although we fully recognize the importance of false discovery rate (FDR) correction in minimizing false positives in high-throughput datasets, applying strict FDR thresholds substantially narrowed the candidate pool, limiting the detection of subtle yet biologically meaningful RI events. To address this, we employed a more inclusive strategy based on nominal p-values ($P < 0.05$) and fold-change cutoffs, which enabled the identification of early splicing alterations. Importantly, several key RI-containing transcripts were subsequently validated by qPCR, reinforcing their biological relevance. Nevertheless, we acknowledge that the use of unadjusted p-values introduces a risk of false positives. Future studies with larger sample sizes and more stringent, FDR-adjusted pipelines will be essential to enhance statistical power, reproducibility, and biomarker development.

Additional investigations using more notable cohorts of independent peripheral blood mononuclear cells from individuals with AD are essential to acquiring a comprehensive understanding of the intricate AS networks involved in this neurodegenerative disorder. Pursuing this objective in future academic endeavors is a formidable challenge. The functional roles of several AS isoforms and their potential influence on AD remain uncertain. Examining splicing dysregulation in AD could improve our current understanding of this complicated condition. Additionally, identifying novel disease biomarkers has been associated with the pathophysiology of other neurodegenerative diseases. This study identifies early RI events in phototransduction-related genes as a potential molecular biomarker in the retina for the early detection of AD, supported by functional deficits observed through ERG analysis.

Data availablity

RNA-seq data used in this study are deposited in the Gene Expression Omnibus (GEO) under the accession number GSE274214.

Received: 7 April 2025; Accepted: 8 July 2025
Published online: 15 July 2025

References

1. Bertram, L., Lill, C. M. & Tanzi, R. E. The genetics of Alzheimer disease: back to the future. *Neuron* **68**, 270–281. https://doi.org/10.1016/j.neuron.2010.10.013 (2010).
2. Long, J. M. & Holtzman, D. M. Alzheimer disease: An update on pathobiology and treatment strategies. *Cell* **179**, 312–339. https://doi.org/10.1016/j.cell.2019.09.001 (2019).
3. Fischer, A. Epigenetic memory: the Lamarckian brain. *EMBO J.* **33**, 945–967. https://doi.org/10.1002/embj.201387637 (2014).
4. Biamonti, G. et al. Alternative splicing in Alzheimer's disease. *Aging Clin. Exp. Res.* **33**, 747–758. https://doi.org/10.1007/s40520-019-01360-x (2021).
5. Farhadieh, M. E. & Ghaedi, K. Analyzing alternative splicing in Alzheimer's disease postmortem brain: a cell-level perspective. *Front. Mol. Neurosci.* **16**, 1237874. https://doi.org/10.3389/fnmol.2023.1237874 (2023).
6. De Strooper, B. & Karran, E. The cellular phase of Alzheimer's disease. *Cell* **164**, 603–615. https://doi.org/10.1016/j.cell.2015.12.056 (2016).
7. Canter, R. G., Penney, J. & Tsai, L. H. The road to restoring neural circuits for the treatment of Alzheimer's disease. *Nature* **539**, 187–196. https://doi.org/10.1038/nature20412 (2016).
8. Chen, X. & Holtzman, D. M. Emerging roles of innate and adaptive immunity in Alzheimer's disease. *Immunity* **55**, 2236–2254. https://doi.org/10.1016/j.immuni.2022.10.016 (2022).
9. Deschenes, M. & Chabot, B. The emerging role of alternative splicing in senescence and aging. *Aging Cell* **16**, 918–933. https://doi.org/10.1111/acel.12646 (2017).
10. Baralle, F. E. & Giudice, J. Alternative splicing as a regulator of development and tissue identity. *Nat. Rev. Mol. Cell. Biol.* **18**, 437–451. https://doi.org/10.1038/nrm.2017.27 (2017).
11. Adusumalli, S., Ngian, Z. K., Lin, W. Q., Benoukraf, T. & Ong, C. T. Increased intron retention is a post-transcriptional signature associated with progressive aging and Alzheimer's disease. *Aging Cell* **18**, e12928. https://doi.org/10.1111/acel.12928 (2019).
12. Ong, C. T. & Adusumalli, S. Increased intron retention is linked to Alzheimer's disease. *Neural Regen. Res.* **15**, 259–260. https://doi.org/10.4103/1673-5374.265549 (2020).
13. Li, D., McIntosh, C. S., Mastaglia, F. L., Wilton, S. D. & Aung-Htut, M. T. Neurodegenerative diseases: a hotbed for splicing defects and the potential therapies. *Transl. Neurodegener.* **10**, 16. https://doi.org/10.1186/s40035-021-00240-7 (2021).
14. Sun, Y. et al. A splicing transcriptome-wide association study identifies novel altered splicing for Alzheimer's disease susceptibility. *Neurobiol Dis.* **184**, 106209. https://doi.org/10.1016/j.nbd.2023.106209 (2023).
15. Li, S., Liu, B., Zhang, L. & Rong, L. Amyloid beta peptide is elevated in osteoporotic bone tissues and enhances osteoclast function. *Bone* **61**, 164–175. https://doi.org/10.1016/j.bone.2014.01.010 (2014).
16. Stakos, D. A. et al. The Alzheimer's disease amyloid-beta hypothesis in cardiovascular aging and disease: JACC focus seminar. *J. Am. Coll. Cardiol.* **75**, 952–967. https://doi.org/10.1016/j.jacc.2019.12.033 (2020).
17. Hart, N. J., Koronyo, Y., Black, K. L. & Koronyo-Hamaoui, M. Ocular indicators of Alzheimer's: exploring disease in the retina. *Acta Neuropathol.* **132**, 767–787. https://doi.org/10.1007/s00401-016-1613-6 (2016).
18. Jindal, V. Interconnection between brain and retinal neurodegenerations. *Mol. Neurobiol.* **51**, 885–892. https://doi.org/10.1007/s12035-014-8733-6 (2015).
19. London, A., Benhar, I. & Schwartz, M. The retina as a window to the brain-from eye research to CNS disorders. *Nat. Rev. Neurol.* **9**, 44–53. https://doi.org/10.1038/nrneurol.2012.227 (2013).
20. Gaire, B. P. et al. Alzheimer's disease pathophysiology in the retina. *Prog. Retin. Eye Res.* **101**, 101273. https://doi.org/10.1016/j.preteyeres.2024.101273 (2024).
21. Coppola, G. et al. Optical coherence tomography in Alzheimer's disease: A meta-analysis. *PLoS ONE* **10**, e0134750. https://doi.org/10.1371/journal.pone.0134750 (2015).
22. Danesh-Meyer, H. V., Birch, H., Ku, J. Y., Carroll, S. & Gamble, G. Reduction of optic nerve fibers in patients with Alzheimer disease identified by laser imaging. *Neurology* **67**, 1852–1854. https://doi.org/10.1212/01.wnl.0000244490.07925.8b (2006).
23. Risacher, S. L. et al. Visual contrast sensitivity in Alzheimer's disease, mild cognitive impairment, and older adults with cognitive complaints. *Neurobiol. Aging* **34**, 1133–1144. https://doi.org/10.1016/j.neurobiolaging.2012.08.007 (2013).
24. Cronin-Golomb, A. et al. Visual dysfunction in Alzheimer's disease: relation to normal aging. *Ann. Neurol.* **29**, 41–52. https://doi.org/10.1002/ana.410290110 (1991).
25. Koronyo-Hamaoui, M. et al. Identification of amyloid plaques in retinas from Alzheimer's patients and noninvasive in vivo optical imaging of retinal plaques in a mouse model. *Neuroimage* **54**(Suppl 1), S204-217. https://doi.org/10.1016/j.neuroimage.2010.06.020 (2011).
26. Alexandrov, P. N., Pogue, A., Bhattacharjee, S. & Lukiw, W. J. Retinal amyloid peptides and complement factor H in transgenic models of Alzheimer's disease. *NeuroReport* **22**, 623–627. https://doi.org/10.1097/WNR.0b013e3283497334 (2011).
27. Smale, G., Nichols, N. R., Brady, D. R., Finch, C. E. & Horton, W. E. Jr. Evidence for apoptotic cell death in Alzheimer's disease. *Exp. Neurol.* **133**, 225–230. https://doi.org/10.1006/exnr.1995.1025 (1995).
28. Su, J. H., Anderson, A. J., Cummings, B. J. & Cotman, C. W. Immunohistochemical evidence for apoptosis in Alzheimer's disease. *NeuroReport* **5**, 2529–2533. https://doi.org/10.1097/00001756-199412000-00031 (1994).
29. Zhang, J., Gao, F., Ma, Y., Xue, T. & Shen, Y. Identification of early-onset photoreceptor degeneration in transgenic mouse models of Alzheimer's disease. *iScience* **24**, 103327. https://doi.org/10.1016/j.isci.2021.103327 (2021).
30. McAnany, J. J. et al. Rod pathway and cone pathway retinal dysfunction in the 5xFAD mouse model of Alzheimer's disease. *Sci. Rep.* **11**, 4824. https://doi.org/10.1038/s41598-021-84318-2 (2021).
31. Athiraman, U. & Giri, T. Isoflurane preconditioning induced genomic changes in mouse cortex. *BJA Open* **10**, 100268. https://doi.org/10.1016/j.bjao.2024.100268 (2024).
32. Percie du Sert, N. et al. The ARRIVE guidelines 2.0: Updated guidelines for reporting animal research. *J. Cereb. Blood Flow Metab.* **40**, 1769–1777 (2020).
33. Oakley, H. et al. Intraneuronal beta-amyloid aggregates, neurodegeneration, and neuron loss in transgenic mice with five familial Alzheimer's disease mutations: potential factors in amyloid plaque formation. *J. Neurosci.* **26**, 10129–10140. https://doi.org/10.1523/JNEUROSCI.1202-06.2006 (2006).
34. Pinero, J. et al. The DisGeNET knowledge platform for disease genomics: 2019 update. *Nucleic Acids Res.* **48**, D845–D855. https://doi.org/10.1093/nar/gkz1021 (2020).
35. Chang, B. et al. Retinal degeneration mutants in the mouse. *Vis. Res.* **42**, 517–525. https://doi.org/10.1016/s0042-6989(01)00146-8 (2002).

36. Ulland, T. K. et al. TREM2 maintains microglial metabolic fitness in Alzheimer's disease. *Cell* https://doi.org/10.1016/j.cell.2017.07.023 (2017).
37. Zhang, M. et al. Brain and retinal abnormalities in the 5xFAD mouse model of Alzheimer's disease at early stages. *Front. Neurosci.* **15**, 681831. https://doi.org/10.3389/fnins.2021.681831 (2021).
38. Kim, M. J. et al. Transcriptome dynamics of alternative splicing events revealed early phase of apoptosis induced by methylparaben in H1299 human lung carcinoma cells. *Arch. Toxicol.* **94**, 127–140. https://doi.org/10.1007/s00204-019-02629-w (2020).
39. Shen, S. et al. rMATS: robust and flexible detection of differential alternative splicing from replicate RNA-Seq data. *Proc. Natl. Acad. Sci. U. S. A.* **111**, E5593-5601. https://doi.org/10.1073/pnas.1419161111 (2014).
40. Middleton, R. et al. IRFinder: assessing the impact of intron retention on mammalian gene expression. *Genome Biol.* **18**, 51. https://doi.org/10.1186/s13059-017-1184-4 (2017).
41. Li, H. D., Funk, C. C. & Price, N. D. iREAD: a tool for intron retention detection from RNA-seq data. *BMC Genomics* **21**, 128. https://doi.org/10.1186/s12864-020-6541-0 (2020).
42. Vanichkina, D. P., Schmitz, U., Wong, J. J. & Rasko, J. E. J. Challenges in defining the role of intron retention in normal biology and disease. *Semin. Cell. Dev. Biol.* **75**, 40–49. https://doi.org/10.1016/j.semcdb.2017.07.030 (2018).
43. Ning, A., Cui, J., To, E., Ashe, K. H. & Matsubara, J. Amyloid-beta deposits lead to retinal degeneration in a mouse model of Alzheimer disease. *Invest. Ophthalmol. Vis. Sci.* **49**, 5136–5143. https://doi.org/10.1167/iovs.08-1849 (2008).
44. Ashok, A. et al. Retinal degeneration and Alzheimer's disease: An evolving link. *Int. J. Mol. Sci.* https://doi.org/10.3390/ijms21197290 (2020).
45. Sadun, A. A. & Bassi, C. J. Optic nerve damage in Alzheimer's disease. *Ophthalmology* **97**, 9–17. https://doi.org/10.1016/s0161-6420(90)32621-0 (1990).
46. Yuan, A. & Lee, C. S. Retinal biomarkers for Alzheimer disease: The facts and the future. *Asia Pac. J. Ophthalmol. (Phila)* **11**, 140–148. https://doi.org/10.1097/APO.0000000000000505 (2022).
47. An, M. J. et al. Reorganization of H3K9me heterochromatin leads to neuronal impairment via the cascading destruction of the KDM3B-centered epigenomic network. *iScience* **27**, 110380. https://doi.org/10.1016/j.isci.2024.110380 (2024).
48. Zhang, J., Shi, L. & Shen, Y. The retina: A window in which to view the pathogenesis of Alzheimer's disease. *Ageing Res. Rev.* **77**, 101590. https://doi.org/10.1016/j.arr.2022.101590 (2022).
49. Li, K.-C. et al. Human DDIT4L intron retention contributes to cognitive impairment and amyloid plaque formation. *Cell Discovery* **11**, 12 (2025).
50. Bareil, C. et al. Segregation of a mutation in CNGB1 encoding the beta-subunit of the rod cGMP-gated channel in a family with autosomal recessive retinitis pigmentosa. *Hum. Genet.* **108**, 328–334. https://doi.org/10.1007/s004390100496 (2001).
51. Trudeau, M. C. & Zagotta, W. N. Mechanism of calcium/calmodulin inhibition of rod cyclic nucleotide-gated channels. *Proc. Natl. Acad. Sci. U. S. A.* **99**, 8424–8429. https://doi.org/10.1073/pnas.122015999 (2002).
52. Sherman, P. M. et al. Identification and characterization of a conserved family of protein serine/threonine phosphatases homologous to Drosophila retinal degeneration C. *Proc. Natl. Acad. Sci. U. S. A.* **94**, 11639–11644. https://doi.org/10.1073/pnas.94.21.11639 (1997).
53. Hameed, A. et al. Evidence of RPGRIP1 gene mutations associated with recessive cone-rod dystrophy. *J. Med. Genet.* **40**, 616–619. https://doi.org/10.1136/jmg.40.8.616 (2003).
54. Huang, H. et al. Targeted next generation sequencing identified novel mutations in RPGRIP1 associated with both retinitis pigmentosa and Leber's congenital amaurosis in unrelated Chinese patients. *Oncotarget* **8**, 35176–35183. https://doi.org/10.18632/oncotarget.17052 (2017).
55. Roepman, R. et al. The retinitis pigmentosa GTPase regulator (RPGR) interacts with novel transport-like proteins in the outer segments of rod photoreceptors. *Hum. Mol. Genet.* **9**, 2095–2105. https://doi.org/10.1093/hmg/9.14.2095 (2000).
56. van Wijk, E. et al. The DFNB31 gene product whirlin connects to the Usher protein network in the cochlea and retina by direct association with USH2A and VLGR1. *Hum. Mol. Genet.* **15**, 751–765. https://doi.org/10.1093/hmg/ddi490 (2006).
57. Yang, Z. et al. Mutant prominin 1 found in patients with macular degeneration disrupts photoreceptor disk morphogenesis in mice. *J. Clin. Invest.* **118**, 2908–2916. https://doi.org/10.1172/JCI35891 (2008).
58. Ohno, M. Failures to reconsolidate memory in a mouse model of Alzheimer's disease. *Neurobiol. Learn. Mem.* **92**, 455–459. https://doi.org/10.1016/j.nlm.2009.05.001 (2009).
59. Eimer, W. A. & Vassar, R. Neuron loss in the 5XFAD mouse model of Alzheimer's disease correlates with intraneuronal Abeta42 accumulation and Caspase-3 activation. *Mol. Neurodegener.* **8**, 2. https://doi.org/10.1186/1750-1326-8-2 (2013).
60. Lim, J. K. H. et al. Retinal functional and structural changes in the 5xFAD mouse model of Alzheimer's disease. *Front. Neurosci.* **14**, 862. https://doi.org/10.3389/fnins.2020.00862 (2020).

Acknowledgements

The study was supported by Korea Environment Industry & Technology Institute (KEITI) through "Digital Infrastructure Building Project for Monitoring, Surveying and Evaluating the Environmental Health Program" (grant and award number: 2021003330007) funded by Korea Ministry of Environment (MOE). This work also supported by the National Research Foundation of Korea (NRF) grant funded by the Korea government (MIST) (Basic Research Laboratory: NRF-RS-2023-00220089; NRF-2023R1A2C1007657).

Author contributions

Overall scientific conceptualization, J.-W.K.; methodology and investigation, H.-M.L., J.-Y.K., J.K., G.-S.S., A.-R.J., Y.P., C.-H.K., Y.H., J.-H.L. and J.-W.K.; data analysis and scientific comments, H.-M.L., J.-Y.K., J.K., G.-S.S., A.-R.J., Y.P., C.-H.K., Y.H., J.-H.L., K. H. L., S. R. and J.-W.K.; statistical and bioinformatical analysis, J.K., Y.H., J.-Y.K., and J.-W.K.; writing—original draft, H.-M.L., J.-Y.K., J.K., and J.-W.K.; funding acquisition, J.-W.K.; supervision and project administration, J.-W.K.

Declarations

Competing interests

The authors declare no competing interests.

Ethics approval

The animal study protocol was approved by the Institutional Review Board of Chung-Ang University (2020-00061), and the approval date is July 27, 2020.

Consent for publication
All authors agree to the publication of this manuscript.

Additional information
Supplementary Information The online version contains supplementary material available at https://doi.org/10.1038/s41598-025-11065-z.

Correspondence and requests for materials should be addressed to J.-W.K.

Reprints and permissions information is available at www.nature.com/reprints.

Publisher's note Springer Nature remains neutral with regard to jurisdictional claims in published maps and institutional affiliations.